DLP Fabrication of Mullite Structures: Flaw Mitigation Through Powder Thermal Processing

ceramics

MDPI

Article

DLP Fabrication of Mullite Structures: Flaw Mitigation Through Powder Thermal Processing

Arianna Bertero [1,*], Bartolomeo Coppola [1], Laura Montanaro [1], Matteo Bergoglio [2], Paola Palmero [1] and Jean-Marc Tulliani [1]

[1] Department of Applied Science and Technology, Politecnico di Torino, INSTM R.U. Lince, 10129 Torino, Italy; bartolomeo.coppola@polito.it (B.C.); laura.montanaro@polito.it (L.M.); paola.palmero@polito.it (P.P.); jeanmarc.tulliani@polito.it (J.-M.T.)

[2] Department of Applied Science and Technology, Politecnico di Torino, Photopolymer Laboratory, 10129 Torino, Italy; matteo.bergoglio@polito.it

* Correspondence: arianna.bertero@polito.it

Abstract

Digital Light Processing (DLP), which operates through a layer-by-layer deposition, has proven to be a promising technique for obtaining complex and customized architectures. However, there are still numerous unresolved challenges in ceramics additive manufacturing, among which is delamination due to suboptimal adhesion between the layers, which threatens the structural integrity and properties of samples. According to recent findings, excess surface hydroxyl groups were identified as being responsible for this defect; a suitable calcination pre-treatment of the ceramic powder could be effective in significantly mitigating delamination flaws in mullite DLP printed bodies. Therefore, in addition to optimizing the printable slurry formulation and printing parameters (mainly in terms of curing energy and layer resolution), this work aimed at investigating the influence of the calcination of a commercial mullite powder (added with magnesium nitrate hexahydrate, as a precursor of the sintering aid MgO) as a simple and effective treatment to additively shape ceramic bodies with limited flaws and enhanced density. The surface characteristics evolution of the mullite powder was investigated, specifically comparing samples after magnesium nitrate hexahydrate addition and ball-milling in water (labeled as BM), and after an additional calcination (BMC). In particular, the effect of the superficial -OH groups detected by FTIR analysis in the BM powder, but not in the BMC sample, was studied and correlated to the properties of the respective ceramic slurry in terms of rheological behavior and curing depth. The hydrophilicity of BM powders, due to superficial hydroxyls groups, affects ceramic powder dispersion and wettability by the resin, causing a weak interface. At the same time, it promotes photopolymerization of the light-sensitive resin, thus inducing the as-printed matrix embrittlement. Anyhow, its photopolymerization degree, equal to 67% and 55% for BM and BMC, respectively, was enough to guarantee the printability of both slurries. However, the use of BMC significantly reduced flaw occurrence in the as-printed bodies and the final density of the samples sintered at 1450 °C (without an isothermal step) was increased (approx. 60% and 50% of the theoretical value for BMC and BM, respectively). Thus, the target porosity of the ceramic bodies was guaranteed, and their structural integrity achieved without any increase in sintering temperature but with a simple powder treatment.

Keywords: ceramics additive manufacturing; digital light processing; mullite; calcination; photopolymerization; conversion rate; delamination; acrylic group; hydroxyl groups

Academic Editor: Angel L. Ortiz

Received: 24 December 2025
Revised: 19 January 2026
Accepted: 20 January 2026
Published: 23 January 2026

1. Introduction

Digital Light Processing (DLP) has demonstrated the possibility of producing ceramic parts with high dimensional accuracy and surface quality through layer-by-layer deposition: the print is produced by consecutively photopolymerizing transverse layers with a thickness from 10 to 200 μm, thus achieving a *z*-axis resolution in the tenths of micrometers [1–4]. Therefore, the penetration of UV light through the slurry is a key aspect of the printing performance [5,6]. However, the penetration depth is limited by the presence of ceramic particles, which have a different refractive index (RI) than the photosensitive resin. Slurries for DLP contain between 35 and 65 vol% of photosensitive resins [7–10], which are generally acrylic-based, either commercially produced or home-made formulated [11–15]. The formulation of ceramic slurries requires careful optimization. In particular, the solid loading is a crucial parameter: a too high ceramic particle load could cause high UV light scattering, reducing the curing depth and hindering good adhesion between the layers. Moreover, the viscosity could be too high to achieve suitable slurry spreadability for layer production. In addition, the solid load of a ceramic slurry must be sufficiently high to ensure a good densification of the sintered part. Finally, it should be noted that to densify the printed parts, it is first necessary to remove the resin from the printed samples by chemical (in water or solvent) and thermal debinding processes, before sintering. The debinding phase is a very sensitive step: gas and bubble formation can occur, promoting interlayer delamination and cracking during sintering [1,8,16].

Thus, although the DLP technique provides numerous advantages, it is still a great challenge to effectively fabricate defect-free parts, while delamination cracks and anisotropy in the final objects is frequently observed [6,17–27]. To address these limitations, several studies have been conducted to improve the quality of DLP-printed components. Some studies focused on optimizing thermal post-treatment. In particular, several investigations on the debinding of the as-printed bodies were conducted [1,8,28]. For instance, Cramer et al. [19] has developed a more gradual thermal debinding protocol on alumina films than the commercial heating cycle in order to realize defect-free large parts. Lam et al. [25] optimized the thermal debinding step to reduce pressure build-up in DLP-printed bodies using commercial alumina slurries, obtaining a reduction of 83% in the average delamination and increasing the thickness of the final parts. Also, the crucial sintering step of additively manufactured ceramic components is increasingly being studied and optimized [22,26]. Other studies focused on ceramic slurry formulation and characteristics, crucial to limiting after-printing defects. For example, Komissarenko et al. [29] studied the production of dense zirconia samples by modulating the dopant percentage and rheology of the slurry. The interaction of the printable slurry with UV radiation is critical in the production of defective free bodies. Peterson et al. [18] developed functionally graded structures by controlling the interlaminar adhesion and spatial density of crosslinking using UV light modulation. Indeed, light scattering penalizes the curing depth and, consequently, the quality of the as-printed bodies can be limited, controlling the refractive index mismatch between the filler and resin [6,21,30], as well as the particle size and distribution [31]. Xie et al. [17] used the finite-difference time-domain (FDTD) method to study the influence of the resin refractive index, the filler refractive index, and the filler particle size on the spatial and temporal evolution of the degree of conversion.

The study of superficial properties of ceramic powders is an innovative approach gaining increasing attention. A recent study on ceria-stabilized zirconia investigated how pre-treatment methods influence powder dispersion, slurry stability, and layer curing, proving the high potential of ceramic powder calcination to improve the final densification and mechanical performance of DLP-printed components [32]. This effective and simple strategy has not been applied to other ceramic systems so far and further investigation is

recommended to confirm the validity of this strategic approach for other compositions as well. Thus, the current study aims to demonstrate the crucial role of the surface chemistry of mullite, a refractory material with characteristics, such as high durability and high thermal shock resistance [33–36], which make it desirable in different sectors, including for high-temperature applications [37], in sensor technology [38], or to produce substrates for carbon dioxide (CO_2) capture [39–41]. The present research investigates the differences in behavior between uncalcined and calcined mullite powders during the production of additively manufactured mullite substrates. These substrates are designed to retain residual porosity to enable the deposition and adhesion of metal–organic framework crystals able to bond CO_2 molecules, such as HKUST-1 [40], thereby serving as robust and high-surface-area architectures for gas filtration and CO_2 capture applications [39,41–43]. The targeted application mullite-based architectures must combine a flawless microstructure and sufficient mechanical integrity with high open porosity. Recent studies on DLP-printed mullite supports for CO_2 capture show that substrates with higher total and open porosity promote more homogeneous and extensive MOF functionalization, underlining the importance of an accessible pore network for gas transport and precursor infiltration [39–41]. In porous mullite ceramics produced both via additive or more traditional manufacturing strategies [42,43], porosity values in the range of ~35–45% have been associated with an effective balance between mechanical strength and permeability, which are desirable characteristics for sensors, refractory supports, and CO_2 capture substrates. In particular, in the current work, a mullite ball-milled powder with added magnesium nitrate hexahydrate as a precursor of the sintering aid MgO (labeled as BM) and the same powder but additionally submitted to calcination (labeled as BMC) were investigated. Results in terms of chemical (by means of the X-ray fluorescence technique, XRF) and surface (by means of Fourier-Transformed Infrared spectroscopy, FTIR) analyses of the powders, slurry rheology, depth of polymerization, and degree of slurry conversion (followed by Attenuated Total Reflectance Fourier-Transformed Infrared spectroscopy, FTIR-ATR) are provided, together with density and microstructural characterizations of the as-printed and sintered samples.

2. Materials and Methods

2.1. Mullite Powder: Treatments and Characterizations

Ceramic samples were obtained from a commercial mullite powder (JMS-70, Jiangsu Jingxin New Material Co., Ltd., Luoyang, China) supplied by Saint-Gobain Research Provence and were produced by sintering from high-purity raw materials, including industrial alumina and kaolin [44]. To reduce the mean particle size and narrow the particle size distribution, the mullite powder was ball-milled with zirconia spheres in water for 48 h. The weight ratios used were 6:1 for zirconia spheres to mullite and 2:1 for water to mullite. Magnesium nitrate hexahydrate $Mg(NO_3)_2{\cdot}6H_2O$ (Sigma-Aldrich, Milan, Italy, 99.0% purity) was added as a precursor of the sintering aid (MgO) at 1 wt% ratio [45]. To guarantee the best comminution efficiency, the optimal speed ωn (85 rpm) was calculated according to Bond's critical speed formula [46]. Then, ball-milled (BM) powders were calcined at 650 °C for 1 h (BMC; heating ramp of 10 °C/min), to obtain the thermal decomposition of $Mg(NO_3)_2{\cdot}6H_2O$ into the desired oxide form [47].

Mullite powders in the as-received, BM, and BMC form were characterized by laser granulometry (Mastersizer 3000, Malvern Pan'alytical, Great Malvern, UK), providing cumulative and differential granulometric data to evaluate their particle size distribution and the average particle size (D_{50}). A Field-Emission Scanning Electron Microscope (FESEM) Hitachi S4000 (Tokyo, Japan) was used to study the powders' morphology. The phase composition was determined by X-Ray Diffraction (XRD, Empyrean, Malvern Pan'alytical, Great Malvern, UK) with CuKα radiation (λ = 0.154056 nm) in the 2θ range 5–70°. A

time per step of 22.95 s and step size of 0.0066° were used. Further details on power characterizations are detailed in a previous work [40].

2.2. DLP Printing of Mullite Samples, Post Processes, and Sintering

Both BM and BMC mullite powders were mixed separately with a photosensitive commercial resin (Admatec Europe BV, Alkmaar, The Netherlands) consisting of acrylate-based monomers containing the photoinitiator diphenyl(2,4,6-trimethylbenzoyl) phosphine oxide (TPO). Based on previous studies [39–41], a solid loading of 69 wt% was selected, with 5 wt% (compared to the mullite content) of commercial dispersant (Disperbyk-103, BYK Chemie, Wesel, Germany). Then, after mechanical stirring, the slurry was homogenized in agate jars with agate spheres (d = 10 mm) for 6 h at 350 rpm in a planetary miller (Fritsch Pulverisette, Fritsch GmbH, Idar-Oberstein, Germany). Vacuum degassing using a rotary pump to remove air bubbles was performed for 30 min before the printing job. The rheological behavior of the slurries was analyzed at 25 °C with a rotational rheometer (Kinexus Pro+, Netzsch Gerätebau GmbH, Selb, Germany) equipped with stainless-steel parallel plates (20 mm in diameter), with a 1 mm gap between plates at shear rates ranging between 0.1 and 1000 s^{-1}.

A DLP-based stereolithographic printer (Admaflex 130, Admatec Europe BV, Alkmaar, The Netherlands) operating with a 405 nm wavelength UV light was used. The slurry was spread on a moving tape through a 125 μm doctor blade. Good resolution, layer adhesion, and uniformity were guaranteed by preliminary investigations on single-layer photopolymerization; curing depth tests, as detailed below, allowed an accurate optimization of the printing parameters.

The curing depth of a single layer was determined for both BM and BMC slurries, exposing them to the UV lamp of the Admaflex 130 machine, equipped with a high-power WQXGA light engine with 2560 × 1600 pixels [48]. Irradiation was performed at different energy per unit area (mJ/cm^2), tuning the time exposure (1, 1.5, 2, 2.5, 3, and 3.5 s) and LED power (13.93, 17.09, and 20.24 mW/cm^2). The cured layers in a chessboard configuration were cleaned with paper to remove the uncured slurry, and the thickness of the single layer was measured with a digital micrometer. The optimal parameters ensure both good squares resolution and a curing depth at least 3 times the set layer thickness.

Thus, the following specifications were set for both BM and BMC slurries: a printing layer thickness of 30 μm, exposure time of 1.5 s, 17.09 mW/cm^2 as LED power, and a delay before exposure of 20 s. Samples with two different geometries were additively manufactured: pellets (nominal diameter of 10 mm and 2 mm in height) and bars (15 mm × 5 mm × 2 mm). The correspondent digital model in the form of files in Standard Tessellation Language (.stl) were designed by AutoCAD 2018 software (Autodesk, San Francisco, CA, USA).

As-printed bodies were left in water overnight at 30 °C: the water debinding process has the aim to remove uncured slurry as well as the hydro-soluble components of the resin. After careful drying in an oven at 70 °C overnight, samples were submitted to thermal debinding and sintering processes according to the treatment employed in our previous work [39]. Thermal treatments were performed in an electric furnace (Nabertherm, Nabertherm GmbH, Lilienthal, Germany) under air atmosphere; a sintering temperature of 1450 °C was set.

Geometrical density ρ (g/cm^3) was determined by mass and geometric measurements for both as-printed samples (after water debinding) and sintered bodies; Archimedes' density was determined by the buoyancy method, following Archimedes' principle (Density Determination Kit, Sartorius YDK01, Göttingen, Germany). Both densities were then related to the theoretical density (TD) of mullite (δ_{TH}, 3.17 g/cm^3 [45]). Sintered samples were also

characterized in terms of porosity. The total and the closed porosity are considered as the hundredth complement of the geometrical and Archimedes' density, respectively, expressed as a percentage of the theoretical mullite density [$(1-\delta/\delta_{TH}) \times 100$]. Furthermore, the microstructures of sintered and as-printed bodies were characterized by means of FESEM observations after platinum sputtering (Q150T S, Quorum Technologies, Lewes, UK).

To evaluate the interaction between $Mg(NO_3)_2 \cdot 6H_2O$ and the resin, an amount of salt equivalent to 1 wt% of MgO with respect to mullite and 5 wt% of dispersant were added to the resin in the absence of ceramic powder. A single layer was obtained in the solid configuration after irradiating the samples for 4 s at 17.09 mW/cm^2. After water debinding overnight and drying, the microstructure was evaluated by means of FESEM observations and compared with an equivalent control sample made up of blank resin.

2.3. Fourier-Transform Infrared Spectroscopy (FTIR)

FTIR measurements (Nicolet iS 50 Spectrometer, Thermo Fisher Scientific, Milan, Italy) on ceramic powders, liquid resin, and as-printed bodies were conducted in transmission mode while ATR mode was used to monitor the curing process. The photopolymerization reaction was investigated on the blank resin itself and on both of the ceramic slurries (BM and BMC). The uncured sample was spread using a stir bar over a silicon slice with a 32 µm thickness. The degree of double bond conversion was evaluated by following the decrease in the characteristic absorption peak of the acrylate double bond (C=C) centered at around 1620 cm^{-1} (C=C). The characteristic absorption peak of the carbonyl group (C=O), centered at 1724 cm^{-1}, was selected as a reference to calculate the conversion rate, eliminating the effect of the sample thickness fluctuations on the intensity of the acrylate absorption peak [11–13,49]. Thus, conversion during irradiation was calculated according to Equation (1) [13,49]:

$$Conversion(\%) = \frac{\left(\frac{A_{group}}{A_{ref}}\right)_{t=0} - \left(\frac{A_{group}}{A_{ref}}\right)_{t}}{\left(\frac{A_{group}}{A_{ref}}\right)_{t=0}} \times 100 \quad (1)$$

where A_{group} corresponds to the acrylate group area investigated and A_{ref} is the reference area at 1724 cm^{-1}. Data were collected with a spectral resolution of 4 cm^{-1} and processed using the OMNIC software (version 6.2) from Thermo Fisher Scientific.

3. Results and Discussion

3.1. Powder Characterization

Laser particle size analyses and FESEM micrographs (Figure 1) revealed the effect of ball-milling and calcination on the BM and BMC powders, respectively. As expected, ball-milling caused the particle size distribution to shift toward smaller sizes, reaching a D_{50} of ~2.4 µm (instead of 6.6 µm of the as-received powder), barely narrowing the overall distribution (Figure 1A). After ball-milling (Figure 1C), the powders are made of more smooth and rounded morphology compared to the as-received one (Figure 1B). Fine powders are desirable to obtain dense bodies since they enhance packing density and sinterability, which is not the main scope of the present work; however, they have shown to increase slurry viscosity and UV light scattering [31]. Despite these crucial drawbacks, which are limited by BM powder's smoother surfaces and narrower size distribution, larger particles may improve slurry flowability but may reduce final density and resolution. Under the present processing conditions, a D_{50} in the range of 3–5 µm represents a suitable compromise between viscosity, UV light interaction, and final microstructural quality. As expected, calcination at 650 °C/1 h caused a mild agglomeration, which may have a positive effect in terms of rheological behavior and curing depth. The calcined BM powders

resulted in a D_{50} increased up to ca. 4.4 µm (as showed by the granulometric curves in Figure 1A and confirmed by the FESEM micrographs in Figure 1D), which can therefore be considered optimal for the investigated system to guarantee both good printing quality and acceptable sintered density.

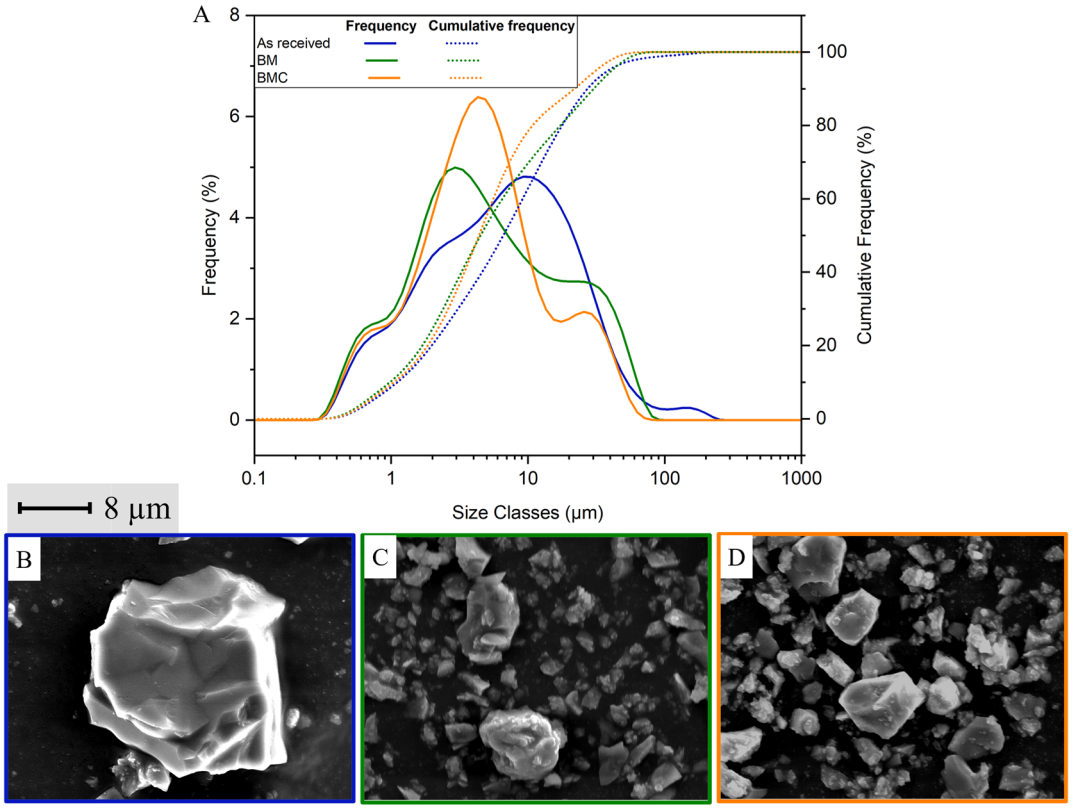

Figure 1. Differential (solid lines) and cumulative (dashed lines) granulometric curves (**A**) and FESEM micrographs of mullite powders in the as-received form (blue curve and (**B**)), after 48 h water ball-milling (BM, green curve and (**C**)), and additional calcination at 650 °C, 1 h (BMC, orange curve and (**D**)) [40].

The XRD patterns of the two mullite powders (Figure 2) are very similar and no differences were found with respect to the as-received one [40]. In all the patterns, mullite (m) and free aluminum oxide (a) peaks were detected, respectively, indexed according to the JCPDS file numbers 15-0776 and 96-900-7499 (hexagonal α-Al_2O_3). As expected, no chemical changes are introduced by calcination when comparing BM and BMC patterns: neither $Mg(NO_3)_2{\cdot}6H_2O$, nor MgO peaks were detected by XRD, since only 1 wt% of sintering aid was employed. Although no Mg-containing crystalline phases were detected by XRD measurements or FESEM observations, magnesium nitrate is expected to decompose completely during the 650 °C calcination step, yielding MgO. Given the very low amount added (1 wt%), Mg is therefore most plausibly present as a highly dispersed nanometric MgO phase or as an ultrathin coating decorating the surface of mullite and alumina particles, rather than as a bulk crystalline phase detectable by diffraction. TEM investigations reported in the literature on commercial mullite powders doped with comparable MgO amounts showed that Mg remains undetectable inside mullite grains and glassy pockets at low and intermediate temperatures, becoming incorporated into the liquid phase only at high sintering temperatures (~1550 °C) [50]. Accordingly, at the calcination temperature employed here, MgO is not expected to react with mullite or alumina and should remain as a separate nanophase decorating the particle surfaces. Furthermore, due to the low calcination temperature and the nanometric nature of MgO, partial surface hydration upon

exposure to ambient humidity may occur, forming a thin $Mg(OH)_2$ layer [51]. MgO is highly reactive toward moisture, but the resulting passivating hydroxide shell limits further hydration, yielding a stable $MgO/Mg(OH)_2$ core–shell structure. Even in small amounts, this surface-localized magnesium phase can alter the particle surface chemistry without affecting the bulk structure, providing a plausible explanation for the observed changes in slurry behavior (Section 3.2).

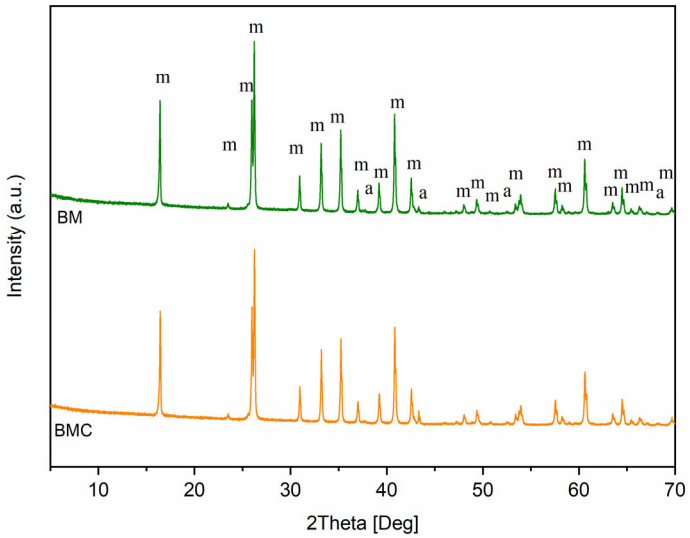

Figure 2. XRD patterns of the ball-milled (BM, green curve) and calcined (BMC, orange curve) powders (m = mullite, a = alumina).

The superficial modifications induced on mullite powders by the milling process and the calcination treatment were highlighted by infrared spectroscopy. This investigation was pivotal to explain the interaction between the mullite powders and the acrylic resin, which plays a crucial role in the formation of flaws and delamination defects in the as-printed samples. With this aim, FTIR measurements (Figure 3) were performed on as-received, ball-milled (BM), and calcined (BMC) mullite powders.

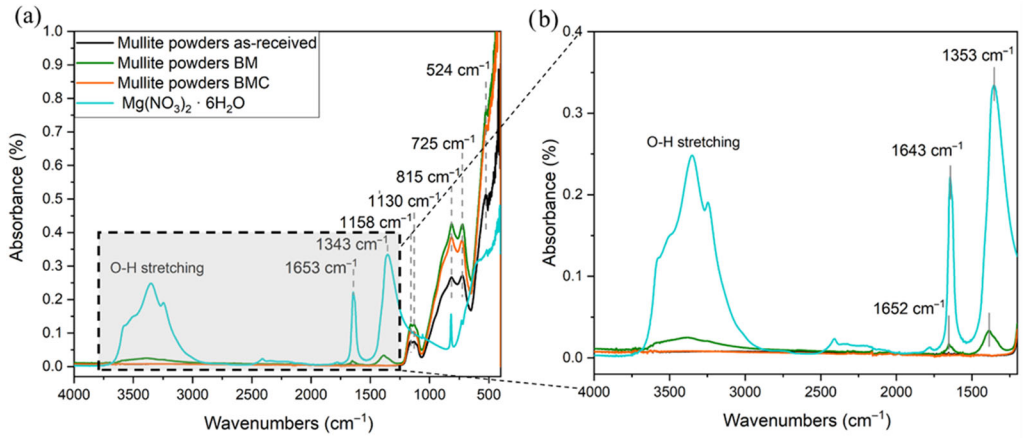

Figure 3. FTIR spectra of as-received (black curve), ball-milled (BM, green curve), and calcined (BMC, orange curve) powders and magnesium nitrate hexahydrate (blue curve): (**a**) full spectrum in the 4000–400 cm^{-1} range; (**b**) enlarged view of the 4000–1200 cm^{-1} region.

Peaks at low wavenumbers are related to mullite-like molecular groups and are present in all the powders. More specifically, the main bands related to the presence of mullite are as follows, according to the literature [52,53]: the SiO_4 (482, 988, 1107, 1131, and

1168 cm^{-1}), AlO_4 (620, 828, and 909 cm^{-1}), AlO_6 (578 and 482 cm^{-1}), and T–O–T (TO_4 where T means Si or Al) (737 cm^{-1}) ones.

Thus, the band at 524 cm^{-1} is ascribed to Al–O stretching vibration modes resulting from AlO_6 groups of mullite (567 cm^{-1} from [54]). The band at 725 cm^{-1} is in agreement with the proposed (Si, Al)–O–(Si, Al) bending mode for the band at 751 cm^{-1} [54] or 737 cm^{-1} [55] in mullite. The peak at 815 cm^{-1} is assigned to AlO_4 (828 cm^{-1}, according to [52,53]). The shoulder around 1158 cm^{-1} is assigned to the vibrational mode of the asymmetric stretch of Si–O–Si (1152 cm^{-1} [54]). Also, 1130 cm^{-1} is a fundamental band assigned to SiO_4 tetrahedra [52,53].

The last three bands, at around 1380, 1650, and between 3000 and 3600 cm^{-1}, occur only in the BM sample. In silicate minerals, bands at around 3400 cm^{-1} and around 1650 cm^{-1} may be attributed to the OH stretching vibrations and the deformation vibration of adsorbed water, respectively [56]. The peak at around 1650 cm^{-1} is also in correspondence with a magnesium nitrate band, so it could be due to the sintering aid as well. Finally, the signal at around 1380 cm^{-1} is associated with the most prominent band of magnesium nitrate at 1353 cm^{-1}, in agreement with the proposed asymmetric stretching mode of NO^{3-} ion (1347 cm^{-1}), according to [57]. The presence of weak signals of the magnesium nitrate is in accordance with the experimental procedure: the sintering aid was mixed with the as-received powder during the ball-milling stage, so it is neither present in the as-received form, nor after calcination. The presence of the nitrate and its hygroscopicity [58] lead to the occurrence of a superficial -OH functional group, which may interfere with the acrylic resin and cause delamination during the water debinding of the as-printed samples. It was verified that the presence of an -OH signal and of the peaks at 1652, 1643, and 1353 cm^{-1} was due to the sintering aid and was not related to the ball-milling procedure, by comparing FTIR spectra of the BM sample with and without the addition of the magnesium nitrate hexahydrate (as reported in the Supplementary Information in Figure S1).

3.2. DLP Process

BMC slurry viscosity is compared with BM slurry (Figure 4). While BMC tends to reach a plateau in the viscosity for high shear rates, the viscosity curve shows a desirable shear thinning behavior at low shear rates, typical of an agglomerated system. After an intermediate phase in which a plateau typical of Newtonian behavior occurs, the high shear rates favor further deagglomeration of the powders, which causes a drop in viscosity. For the BM slurry, the shear thinning behavior starts to occur from a shear rate of 0.1 s^{-1}; thus, higher stresses are required in comparison to the BMC slurry to decrease the viscosity as the shear rate increases. The viscosity of BM remains generally higher than that of BMC, except in the last part of the curve where again the high shear rate favors the flow of both slurries, which thus becomes comparable. Relevant information is the viscosity value at the operative shear rate applied by the blade during slurry spreading (approx. 160 s^{-1}). The BM and BMC slurries show viscosities at 160 s^{-1} of, respectively, 2.03 and 1.31 Pa·s, significantly lower values than 3–5 Pa·s, the limit values guaranteeing suitable flowability for DLP [4,59]. However, it is evident that up to a shear rate of around 200 s^{-1}, BM exhibits a higher viscosity than BMC. In fact, as anticipated in Section 3.1, it is known from the literature that the increase in viscosity and the consequent deterioration in rheological behavior is correlated with a narrower particle size distribution and a smaller particle size. In fact, smaller ceramic particles exhibit an increase in specific surface area and greater mutual attraction [31,60–62]. However, in the case of BM and BMC, the particle size distributions are very similar, and the difference in D_{50} of BMC, although present due to agglomeration during calcination, is small. Therefore, the differences in the surface properties of the two powders can reasonably explain the different viscosity of the slurries;

in fact, the presence of -OH groups on the surface of the BM powders would lead to a greater interaction between the particles, which could explain the slightly higher viscosity of the corresponding slurry. It was already shown how specific superficial treatments of Mg-rich surface layers improving the anti-hydrolysis and dispersion abilities of the ceramic powders, led also to a decrease in viscosity due to the suppression of hydroxyl-driven attractive forces [63]. In our system, the surface passivation mechanism induced by calcination is consistent with the observed decrease in viscosity of the BMC slurry compared to BM, despite their very similar particle size distributions. Therefore, the calcination step does not merely induce mild agglomeration but also alters the surface chemistry of the powder in a way that improves its rheological response during DLP.

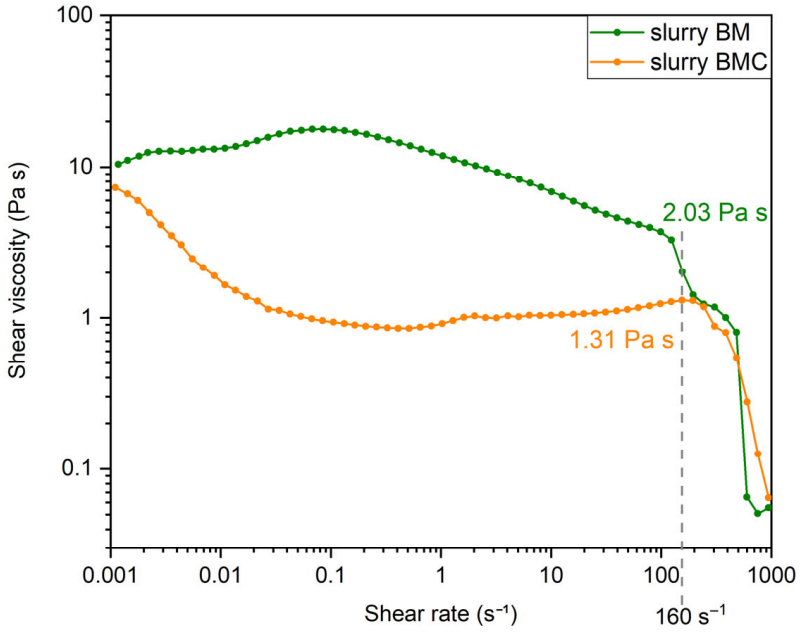

Figure 4. Viscosity curves of mullite slurries prepared with ball-milled (BM, green curve) and calcined (BMC, orange curve) mullite powders, at 69 wt% solid loading and 5 wt% dispersant.

Therefore, although both BM and BMC have rheological behavior compatible with the AM modeling process employed, the BMC slurry results in slightly preferable rheological properties.

Before each printing job, curing depth tests were carried out: the results in terms of layer thickness obtained with different energy per unit area are shown in Figure 5. BM and BMC slurries show very similar curing depths, considering the overlapping of the error bars. However, focusing on the energy window per unit area around the operating value used in the printing jobs (ca. 25.6 mJ/cm^2), slightly higher average thickness values can be seen for the BMC slurry. As anticipated in the granulometric data discussion in Section 3.1, the improved curing behavior observed for the calcined powder can be attributed to a reduction in the effective scattering coefficient, which scales inversely with particle size [31]. However, it is not possible to conclude from the curing depth tests carried out with the 3D printer that a significantly different layer thickness can be achieved with the two slurries at the same delivered energy. For a clearer understanding of the role of the ceramic particles' hydrophilicity degree and their interaction with the resin, FTIR-ATR analyses during the photopolymerization and microstructural analyses of the 3D printed bodies were carried out and are presented below.

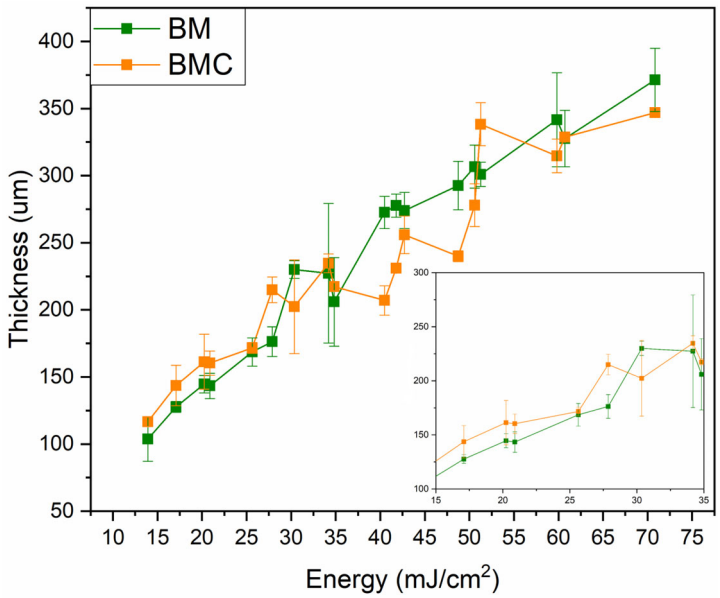

Figure 5. Curing depth tests results for BM and BMC slurries. Error bars are calculated on a minimum of three samples.

FTIR measurements in transmission mode were first performed on the commercial blank resin: the curve shown in Figure 6 is comparable with a typical FTIR spectrum of an acrylic liquid photosensitive resin mixture [49]. The broad peak at approximately 3400 cm^{-1} is due to the hydroxyls groups present in the original formulation of the resin itself. The strong peak at 1724 cm^{-1} is ascribed to the stretching vibrations of C=O, while the characteristic peak centered ca. at 1620 cm^{-1} was assigned to the stretching vibrations of C=C bonds. Stretching vibration of C—O—C bonds are responsible for the peaks at around 1100 cm^{-1} [64]. Finally, the two characteristic peaks at 910 and 810 cm^{-1} were both ascribed to the bending vibrations of C—H bonds. Real-time FTIR tests in ATR mode can be used to evaluate the double bond conversion during irradiation following the acrylic IR peak change: in fact, when exposed to UV irradiation, the unsaturated double bonds are progressively consumed in the radical chain growth reaction with a decrease in the correspondent peak at ca. 1620 cm^{-1} [11–13,49].

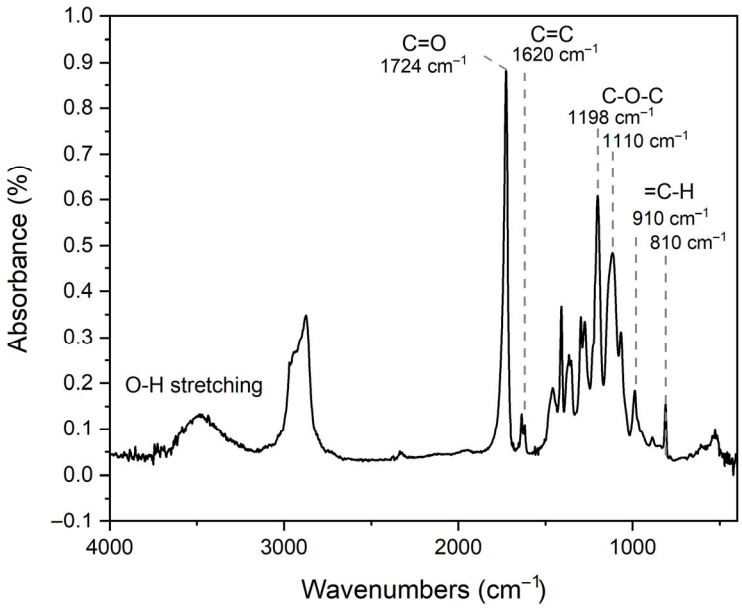

Figure 6. FTIR spectrum of blank commercial resin.

Thus, the progress of the photopolymerization reaction was investigated by means of the FTIR-ATR method for blank resin, which was compared with the two slurries investigated in this study (BM and BMC); the spectra obtained at different irradiation times are shown in Figure 7. The conversion rates (measured by monitoring the decrease in the acrylate peak centered at 1620 cm^{-1}) are reported in Table 1. The FTIR-ATR spectra all show a progressive decrease in the acrylic peak intensity. This phenomenon is well-known in photopolymerization reactions [17,65,66] and attributable to the radical chain growth polymerization reaction. It is evident from the conversion curves that the addition of ceramic particles to the resin causes a drastic inhibition of photopolymerization. In fact, the pristine resin achieves a final conversion above 80%, whereas the formulations containing ceramic powders (either BM or BMC) achieved a conversion of about 60%. This result was expected: the presence of ceramic particles is known to cause scattering phenomena, thus preventing the UV energy from being fully exploited. Furthermore, when comparing the two ceramic slurries with the same particle content, the formulation containing BM powder achieves a higher final conversion. This trend can be appreciated from the lowest irradiation times: indeed, at 60 s, the BMC-filled resin exhibits a 20.8% conversion rate, less than half that of the corresponding BM resin (45%), which is closer to the value of the unfilled resin (50.7%). Prolonging the exposure up to 360 s, the photopolymerization reaction shows a higher progression for the BM slurry than BMC (64.7 vs. 55.9%), although these values are comparable.

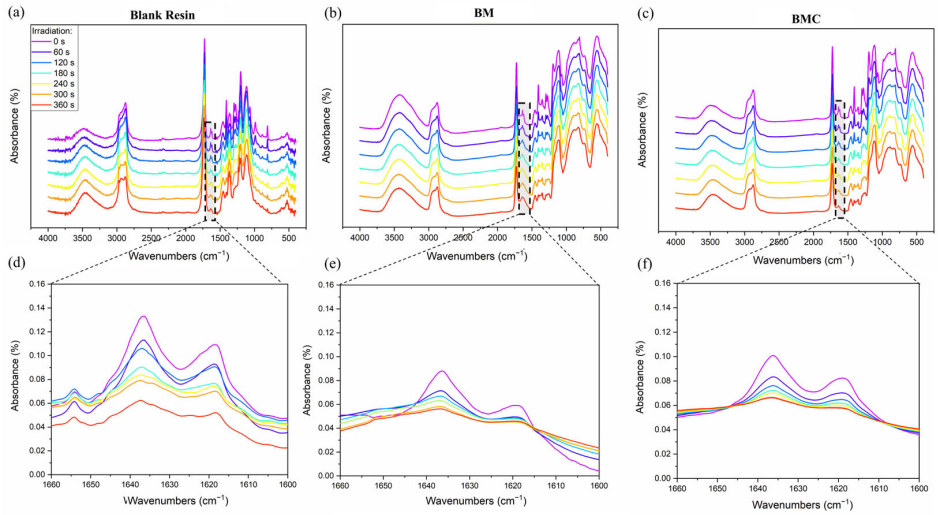

Figure 7. FTIR-ATR measurements for blank resin (**a**,**d**) and BM (**b**,**e**) and BMC (**c**,**f**) slurries for different irradiation times.

Table 1. Conversion percentage of blank resin and BM and BMC slurries with respect to the irradiation time applied during FTIR-ATR measurements.

UV Irradiation (s)	Conversion (%)		
	Blank Resin	BM	BMC
0	0	0.0	0.0
60	50.7	45.0	20.8
120	69.8	56.2	32.7
180	78.5	61.5	41.2
240	80.5	63.8	46.0
300	81.2	66.6	54.0
360	83.9	67.4	55.9

Furthermore, the same analysis was performed for ball-milled powders without sintering aid and no differences with respect to BMC were highlighted (Figure S2). The slightly different behavior in terms of conversion rate between the slurries containing BM and BMC could in fact be related to the surface differences between the two powders and their interaction and distribution in the polymeric matrix. The BM slurry in fact introduces additional -OH groups than those already present in the pristine resin. The presence of the hydroxyl functional groups on the surface of the BM particles gives them greater hydrophilicity than BMC ones, enhancing their wettability by the acrylic resin, which is characterized by pendant polar groups able to form -H bonds with -OH groups on the ceramic surface [67]. It was then proved that hydroxyl-containing acrylate promotes a faster activated monomer mechanism, resulting in increased resin conversion [68]. Thus, polymerization chain reactions proceed with less difficulty in the BM slurry than in the BMC slurry, where ceramic particles scatter UV light, preventing the chain reactions from proceeding. Despite that no relevant differences are highlighted in the curing depth tests, the higher conversion tendency of BM may cause overcuring and consequent embrittlement of the polymeric matrix, enhancing crack formation and propagation in printed bodies [69–71]. This is proposed as a possible explanation of the defects observed in BM samples, as will be explained in the following. On the other hand, the lower BMC conversion has no significant effect on the printability of the slurry; in fact, as seen above, the curing depth values are similar to the results obtained using the UV projector of the Admatec 3D printer (Admaflex 130, Admatec Europe BV, Alkmaar, The Netherlands), if not slightly better for BMC. A good degree of light curing is necessary to ensure sufficient adhesion between the layers to complete the printing job, which was achieved for both slurries. However, this is not sufficient to guarantee good ceramic body quality in both cases, as we shall see below, as this also depends on the interaction of the ceramic particles with the resin.

The FTIR-ATR technique is a very useful technique for understanding the interaction of UV radiation with the slurry and, in particular, with the photosensitive phase; nevertheless, the differences with the instrumentation used for the additive shaping process must be considered. Specifically, on the one hand, in the Admatec Admaflex 130 3D printer, the slurry was spread onto the film with a thickness of 125 μm, while the printer was set to photopolymerize layers of 30 μm; on the other hand, the sample analyzed by FTIR-ATR was only 32 μm thick. Furthermore, for FTIR-ATR a UV lamp with an energy of ca. 75 mW/cm^2 and working wavelength of 385 nm was employed, while the UV source for DLP additive manufacturing operates at 405 nm, irradiating at 17.09 mW/cm^2 for 1.5 s. In any case, FTIR analyses on the BM and BMC as-printed samples (Figure S3) also confirm a higher conversion for BM, but tests on photosensitive slurries are not comparable with as-printed composite bodies, especially after water debinding, since the latter ones reach a significantly higher conversion degree.

3.3. Printed Samples Characterization

Samples additively manufactured from BM slurry showed low superficial quality and delamination after water debinding, in both the geometries realized (Figure 8, top). In particular, water penetration is responsible for the swelling on the surface (Figure 8A) and delamination cracks between the layers (Figure 8B,C). It was indeed observed that delamination did not occur for samples left in air. Nevertheless, water debinding cannot be avoided since it is a crucial step for the development of the final ceramic part: indeed, an efficient debinding process starts from the removal of uncured resin and soluble components. Samples obtained in the printing job performed using slurry with BMC powder (Figure 8D) did not show the defects of the previous samples. In fact, even after water

debinding, no significant layer detachment phenomena were highlighted from optical microscopy (Figure 8F). Thus, the main goal was successfully achieved: delamination was almost totally avoided using calcined mullite powders to manufacture ceramic samples by DLP.

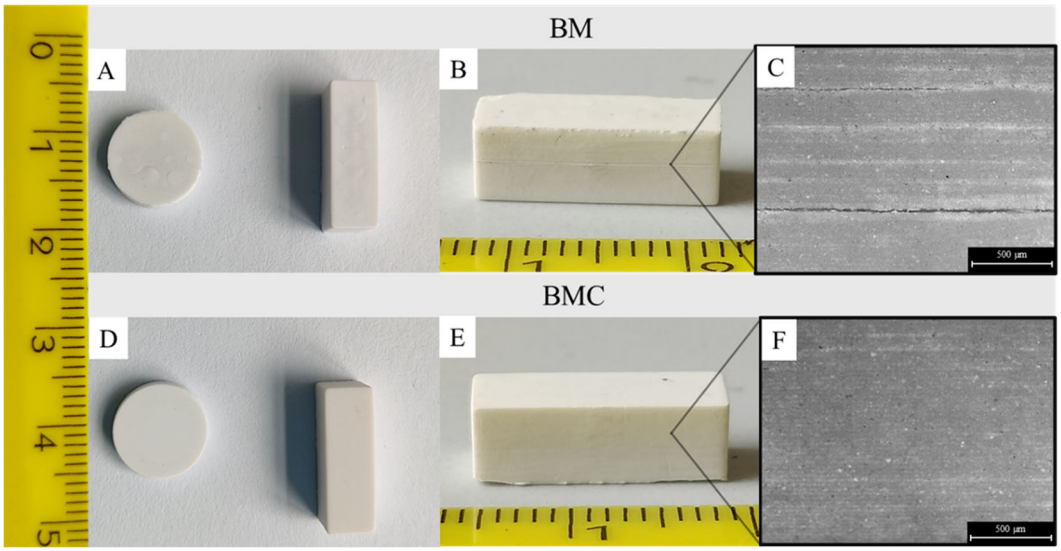

Figure 8. As-printed mullite samples (after water debinding), shaped by DLP using slurries with BM (up) and BMC (down) ceramic powders: pictures from the top (x-y plane, (**A**,**D**)), pictures (**B**,**E**), and optical micrographs (**C**,**F**) of the side (z-x plane).

In Figure 9, FESEM micrographs of the as-printed samples after water debinding are shown; despite that in both cases the light-curing process was effective, BM samples are damaged while the better microstructural quality of the BMC samples is highlighted in terms of both homogeneity and ceramic powder embedding. To definitely exclude the possibility of an artifact, different samples from equivalent printing jobs were analyzed and the reproducibility of the different BM (Figure 9A–C) and BMC (Figure 9D–F) microstructures was confirmed.

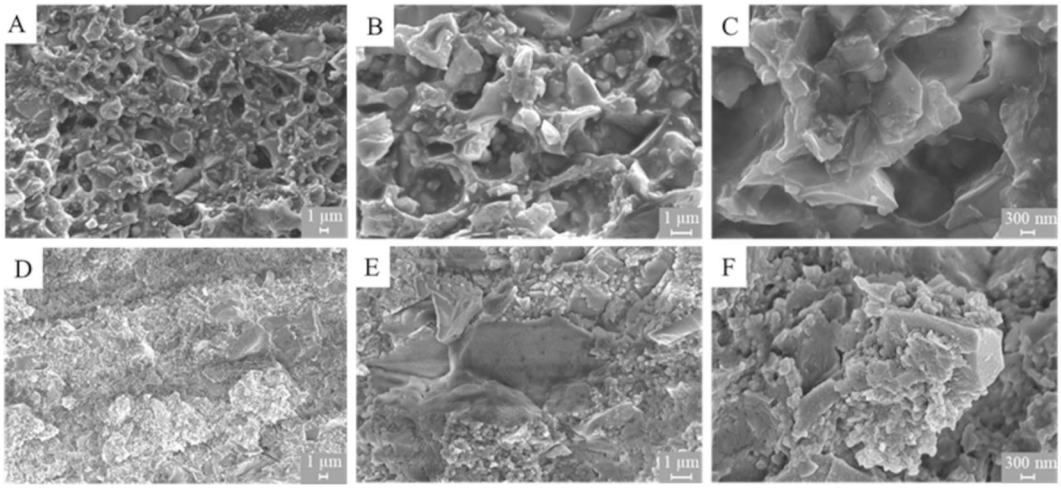

Figure 9. FESEM micrographs of as-printed mullite samples (after water debinding), shaped by DLP using slurries made with BM (**A**–**C**) and BMC (**D**–**F**) ceramic powders.

On the BM fracture surface, voids with an approximately circular shape occur (Figure 9A–C). The same porous microstructure was also observed in samples before water debinding. The nature and cause of the voids were then investigated. In Ref. [72], the

authors demonstrated that a proportion of sub-micron particles of at least 50% is needed to reduce direct contact between bigger particles and to favor the formation of necks during sintering. This particle grading also reduces pores between the printed layers in vat photopolymerized 3D-printed SiC powders. However, the particle size distributions of the BM and BMC powders were very similar, as well as the viscosity value at 160 s^{-1}; thus, the origin of these defects is different. In addition, the presence of powder agglomerates and voids allows the laser beam to penetrate deeper and increase the curing depth [73], but this is not the case in this work as similar curing depths were reached with both powders (Figure 5).

The voids already affected the BM microstructure before water debinding, meaning that they are related to the slurry mixing and printing steps. Assuming a good efficiency of the degassing step and the absence of air bubbles in the slurry, the porous structure is probably caused by the presence of $Mg(NO_3)_2 \cdot 6H_2O$ added to mullite powders during ball-milling. To prove it, the salt was directly mixed with the resin, and persistent granules of $Mg(NO_3)_2 \cdot 6H_2O$ were observed in the monomeric phase. This confirmed the insolubility of this highly hygroscopic salt in the commercial acrylate-based photosensitive resin, which was as expected given the hydrophobic nature of the latter [74]. After curing, water debinding overnight, and drying, it showed the insurgence of pore cavities absent in the resin itself (Figure 10). Indeed, the cured samples made of the resin added with nitrate (Figure 10A–C) showed the same circular cavities than the as-printed ceramic body (Figure 9A–C), while no microstructural porosity occurred with the resin itself (Figure 10D–F). Furthermore, since $Mg(NO_3)_2 \cdot 6H_2O$ is known to be deliquescent, it leads to water vapor molecules adsorption from the atmosphere on the grain powder [75], causing undesired damage of the printed body [76]. The presence of chemisorbed hydroxyls on the surface of ceramic oxides favors the adsorption of a first layer of physiosorbed immobile water molecules followed by a second and a third layer of weakly bound and more mobile molecules with the increase in relative humidity [77]. In the case of porous materials, water condensation is also possible in the capillary-like pores between grains [78], considering the possible agglomeration of the powder observed during rheological measurements. However, the humidity in the room was controlled during the printing step by means of a dehumidification system; therefore, the formation of a liquid film on the surface of grain powders could only occur during the mixing step. Furthermore, since $Mg(NO_3)_2 \cdot 6H_2O$ increases ceramic particles' hydrophilicity, it can also promote the formation of Si-O-C bonds with a dispersant (BYK 103) that are easily hydrolyzed in the presence of moisture, causing a weak interface with the resin and thus favoring water penetration during debinding [67]. As a result, in BM 3D-printed samples during water debinding, water flaws are more prone to propagate due to water penetration in this weak porous microstructure rich in circular voids, resulting in delamination, cracks, and surface bubbles formation, as shown in Figure 8 [16]. Indeed, the debinding steps, both in water and during the subsequent thermal treatment, are crucial, as they must ensure a controlled and gradual decomposition and removal of the resin to prevent the formation of defects and internal cracking [79,80].

In contrast, BMC mullite is less affine to water, resulting in a clearly more homogeneous microstructure after water debinding (Figure 9D). BMC particles are efficiently embedded in the polymerized polymeric matrix (Figure 9E), resulting in a good-quality interface (Figure 9F). These improvements are provided despite the agglomeration caused by calcination. As previously highlighted, a coarser particle size distribution limits UV light scattering but it may lead to less efficient packing and sintering behavior; at the same time, larger particles tend to form agglomerates more easily. Despite that, the slight enlargement of BMC particle size distribution compared to BM does not significantly promote agglomeration in the resin, as proven by FESEM micrographs. However, calcination allows the

removal of -OH groups from ceramic particles surface, reducing their hydrophilicity; in this way, the resin–particle interface is improved and a better embedding in the polymerized matrix is ensured, thus preventing interface damage by water. The diffusion driving force of the water-soluble components of the resin is limited and the water debinding step is more progressive, limiting microstructural defects.

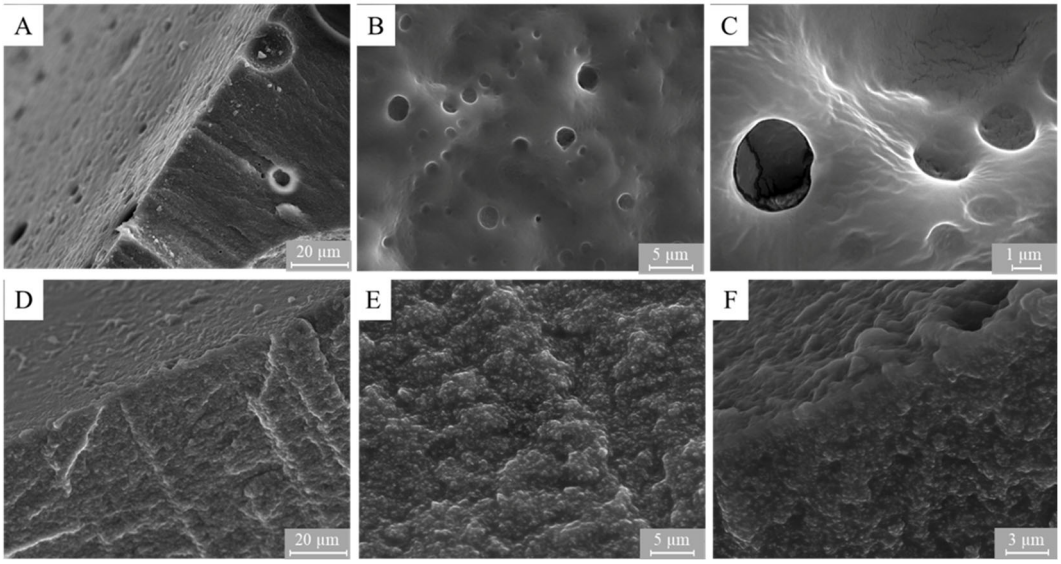

Figure 10. FESEM micrographs of UV-cured layers (after water debinding) of resin with magnesium nitrate hexahydrate (**A**–**C**) and without (**D**–**F**).

Table 2 shows the density and porosity values for the as-printed and sintered bodies. Differences between the BM and BMC printed bodies' geometrical densities are not significant: taking the error bars into account, both achieve composite density values of around 60% compared to the theoretical density, and around 40% considering only the ceramic phase. These results are in accordance with the similar conversion rates reported in Table 1. However, comparing as-printed samples without and with water debinding, a slight but significant reduction in density can be seen in the BM samples after water debinding. This result confirms a higher amount of water-soluble resin components removed from BM samples, where the driving force of water debinding and water penetration is more important due to the highly porous microstructure and higher hygroscopicity of the powders. The final sintered densities definitively highlight the preferable characteristics of the BMC samples: at the same sintering temperature (1450 °C), they achieve a geometric density approximately 18% higher than the corresponding BM samples, as evidenced too by the reduction in the internal porosity (closed porosity approx. 8% vs. 14%, respectively, for BMC and BM). From an application-oriented perspective, these differences are highly relevant. For MOF-functionalized CO_2-capture monoliths, high open porosity is required to ensure efficient MOF deposition and gas transport, whereas closed porosity is ineffective and even detrimental because it reduces the accessible internal volume [39,41–43]. In this context, the BMC samples, which reach a geometric density of ~59%, limiting the closed porosity to ~8%, fall within the typical range of 35–45% reported for porous mullite supports [39,41–43]. Their significantly lower closed porosity indicates that a larger fraction of the pore volume is open and interconnected, which is expected to improve both MOF loading and gas permeability. Therefore, beyond eliminating large defects, calcination promotes a more application-oriented pore architecture, enhancing the suitability of the printed mullite substrates for CO_2 capture, sensing, and related applications.

Table 2. Values of geometrical density and closed porosity percentage for 3D-printed samples (in the as-printed and sintered form) realized with BM and BMC slurries.

			BM	BMC
As-printed	In air	δ_{geom} (%) *	62.8 ± 1.0	59.1 ± 2.5
	After water debinding	δ_{geom} (%) *	60.0 ± 1.0	58.1 ± 4.1
	In respect to the ceramic phase	δ_{geom} (%) *	42.1 ± 1.2	40.1 ± 2.7
Sintered		δ_{geom} (%) *	50.2 ± 1.9	59.3 ± 5.3
		Closed porosity (%)	13.9 ± 2.9	7.7 ± 4.1

* $[\delta/\delta_{TH} \times 100]$.

Sintered parts were observed by the FESEM technique (Figure 11). From the micrographs of the BM printed bodies (Figure 11A,B), it is possible to see significant delamination phenomena in several areas of the sample. Coherently with data shown in Table 2, the magnification in Figure 11C displays a highly porous microstructure where the printing layers are not clearly visible due do the presence of a relatively high amount of internal porosities. Thus, the weak interface of mullite particles and the resin results in a flawed microstructure of the final ceramic bodies. Once again, the advantages of using calcined mullite powders are confirmed. In fact, microstructural defects are almost completely eliminated in BMC samples (Figure 11D–F). Still some signs of interlayer delamination occur (Figure 11D); thus, the next developments need to study the proper strategies for further improvements. The remaining defects are probably due to a suboptimal choice of printing parameters: an increase in the irradiating energy may improve layer adhesion; in other words, a higher LED power and/or exposure time is recommended for future printing jobs with BMC. Alternatively, the increase in the photoinitiator will promote the same scope. To further enhance the structural integrity of the printed bodies, other strategies can also be envisaged as future directions. These include the optimization of the thermal debinding protocol, lowering the heating ramps to minimize internal stress during binder pyrolysis. Finally, the use of a different dispersant may help in achieving better particle packing and stronger resin–ceramic interactions.

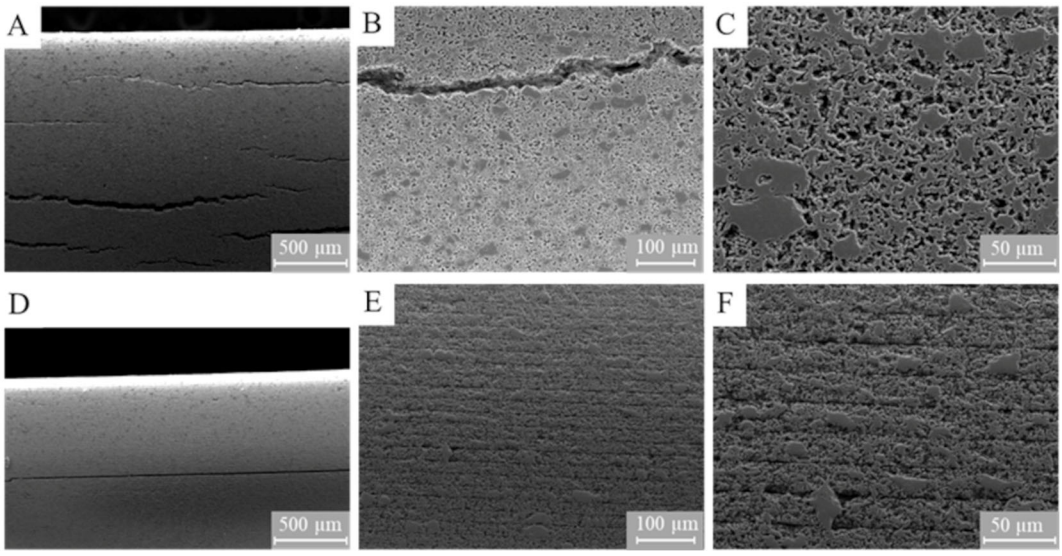

Figure 11. FESEM micrographs of sintered mullite samples, shaped by DLP using slurries with BM (**A**–**C**) and BMC (**D**–**F**) ceramic powders.

Despite the need for further improvements, the micrographs confirm the density data and show a more homogenous and dense sintered body for BMC (Figure 11D), in accordance with the values collected in Table 2. The higher density and lower closed porosity of BMC samples are expected to result in improved mechanical integrity compared to BM samples. However, the benefits in terms of mechanical properties need to be proven with compressive and flexural tests; thus, further printing jobs will focus on the fabrication of proper test specimens with standard sizes and shapes. Mechanical characterizations are beyond the scope of the present work, which demonstrated the benefits of calcination, highlighting a clear microstructural improvement obtained with BMC powders.

4. Conclusions

The effect of calcining mullite powder was studied with the aim of improving the quality of ceramic samples produced additively using the DLP technique.

Mullite powder was added with magnesium nitrate hexahydrate, as a precursor to the sintering aid MgO (1 wt%), and was characterized following ball-milling and calcination. The two powders are compositionally equivalent, while the slight aggregation during calcination is visible from the FESEM micrographs and results in an increase in particle size (D_{50} of 2.4 and 4.4 μm for BM and BMC, respectively). Transmission-mode FTIR analysis revealed the presence of -OH groups on BM powder, introduced by magnesium nitrate hexahydrate and removed during calcination. This affected the properties of the respective ceramic slurries (both made with a solid load of 69% and 5% of a dispersant), primarily the rheological ones. In fact, the slightly higher viscosity of the BM slurry is indicative of a higher interaction between the ceramic particles, due not only to the slightly finer grain size, but also to the presence of surface -OH groups. However, both slurries exhibited a viscosity at an operating shear rate of 160 s^{-1}, compatible with DLP (2.03 and 1.31 Pa·s for BM and BMC slurry, respectively). From the curing depth tests, the average thickness of the BMC layers was comparable to BM; more specifically, at the operating energy window used in the printing jobs (about 25.6 mJ/cm^2), BMC displays slightly higher curing depth. The higher amount of -OH on the BM slurry promotes a polymerization reaction, resulting in a slightly higher conversion compared to BMC (67.4% vs. 55.9%): in both cases, the photopolymerization degree guarantees DLP manufacturing. However, the highly hygroscopic $Mg(NO_3)_2 \cdot 6H_2O$, added during ball-milling as precursor of the sintering aid MgO, makes the ceramic particles' surface poorly wettable in contact with the hydrophobic resin; consequently, the insurgence of important spherical cavities occurs in the microstructure of BM as-printed samples. Furthermore, the weak interface between BM and the resin is easily damageable by water penetration during water debinding. This is confirmed by the slightly higher water-soluble portion of resin removed from BM after water debinding, with a decrease in as-printed body density by about 2% respect to BMC. BM ceramic bodies showed clear signs of surface swelling and of interlayer delamination already in the as-printed form, which were exacerbated following the thermal debinding and sintering processes. In contrast, the calcination process allowed us to remove the -OH group from the ceramic surface, decreasing the powder's hygroscopicity. Thus, in BMC samples, calcined powders were probably better dispersed into the polymer matrix, and the microstructure of the as-printed BMC samples was clearly more homogenous. Indeed, the density of the final sintered samples definitively highlighted the advantages provided by calcined mullite powders: at the same sintering temperature (1450 °C), BMC samples achieved higher geometric density compares to BM samples (respectively, ca. 60% vs. 50% compared to the theoretical density of mullite). Consequently, the FESEM micrographs of sintered bodies displayed dramatic delamination and highly porous microstructure in BM samples. On the other side, microstructural defects were almost eliminated in BMC

samples, which clearly appeared more homogenous and denser. Further developments will require flexural and compressive tests to prove the effect on mechanical properties. Some signs of interlayer delamination still occurred, which can be mitigated in the future with different possible strategies (a deeper optimization of printing parameters, formulation, or thermal treatments). However, the resulting denser and more homogeneous microstructure, with reduced closed porosity, is expected to improve the functional performance of the printed bodies in applications such as CO_2 capture, sensors, and refractory supports. The current work provides evidence of the advantages obtained with the calcination of mullite powders and of the importance of a careful selection of the sintering aids employed in DLP ceramic manufacturing.

Supplementary Materials: The following supporting information can be downloaded at: https://www.mdpi.com/article/10.3390/ceramics9020011/s1, Figure S1: FTIR patterns of mullite powders' ball-milled form with (green curve) and without the sintering additive (pink curve), and the sintering additive itself (magnesium nitrate hexahydrate, blue curve); Figure S2: ATR-FTIR measurements for ceramic slurry realized with mullite powders ball-milled without $Mg(NO_3)2{\cdot}6H_2O$ additive; Figure S3: FTIR measurements of as-printed bodies after water debinding and drying. Comparison between samples realized with ball-milled (BM, green curve) and calcined (BMC, orange curve) mullite powders.

Author Contributions: Conceptualization, P.P. and J.-M.T.; Methodology, B.C., A.B. and M.B.; Formal Analysis, A.B.; Investigation, A.B. and B.C.; Data Curation, B.C., P.P. and J.-M.T.; Writing—Original Draft, A.B.; Writing—Review and Editing, B.C., L.M., P.P. and J.-M.T.; Supervision, P.P. and J.-M.T. All authors have read and agreed to the published version of the manuscript.

Funding: This publication is part of the project NODES, which has received funding from the MUR—M4C2 1.5 of PNRR funded by the European Union—NextGenerationEU (Grant agreement no. ECS00000036).

Data Availability Statement: The original contributions presented in the study are included in the article/Supplementary Material, further inquiries can be directed to the corresponding author.

Acknowledgments: The authors greatly acknowledge the interdepartmental laboratory SISCON (Safety of Infrastructures and Constructions) from Politecnico di Torino for the use of the rheometer. Special acknowledgements to Saint-Gobain Research Provence for the supply of mullite powders. The authors also gratefully acknowledge Marco Sangermano (Politecnico di Torino) for access to and assistance with the FTIR equipment.

Conflicts of Interest: The authors declare no conflicts of interest.

References

1. Olhero, S.M.; Torres, P.M.C.; Mesquita-Guimarães, J.; Baltazar, J.; Pinho-da-Cruz, J.; Gouveia, S. Conventional versus Additive Manufacturing in the Structural Performance of Dense Alumina-Zirconia Ceramics: 20 Years of Research, Challenges and Future Perspectives. *J. Manuf. Process* **2022**, *77*, 838–879. [CrossRef]
2. Santoliquido, O.; Colombo, P.; Ortona, A. Additive Manufacturing of Ceramic Components by Digital Light Processing: A Comparison between the "Bottom-up" and the "Top-down" Approaches. *J. Eur. Ceram. Soc.* **2019**, *39*, 2140–2148. [CrossRef]
3. Mamatha, S.; Biswas, P.; Johnson, R. Digital Light Processing of Ceramics: An Overview on Process, Materials and Challenges. *Prog. Addit. Manuf.* **2023**, *8*, 1083–1102. [CrossRef]
4. Fiume, E.; Coppola, B.; Montanaro, L.; Palmero, P. Vat-Photopolymerization of Ceramic Materials: Exploring Current Applications in Advanced Multidisciplinary Fields. *Front. Mater.* **2023**, *10*, 1242480. [CrossRef]
5. Zakeri, S.; Vippola, M.; Levänen, E. A Comprehensive Review of the Photopolymerization of Ceramic Resins Used in Stereolithography. *Addit. Manuf.* **2020**, *35*, 101177. [CrossRef]
6. Li, Y.; Huang, S.; Wang, S.; Zhang, X.; Wang, Y.; Lu, B.; Luo, Y.; He, F.; Liu, W.; Wu, S. Research on the Effects of Surface Modification of Ceramic Powder on Cure Performance during Digital Light Processing (DLP). *Ceram. Int.* **2022**, *48*, 3652–3658. [CrossRef]

7. Gu, Q.; Sun, L.; Ji, X.; Wang, H.; Yu, J.; Zhou, X. High-Performance and High-Precision Al_2O_3 Architectures Enabled by High-Solid-Loading, Graphene-Containing Slurries for Top-down DLP 3D Printing. *J. Eur. Ceram. Soc.* **2023**, *43*, 130–142. [CrossRef]
8. Shen, Y.; Sun, Y.; Jin, B.; Li, M.; Xing, B.; Zhao, Z. Effect of Debinding and Sintering Profile on the Optical Properties of DLP-3D Printed YAG Transparent Ceramic. *Ceram. Int.* **2022**, *48*, 21134–21140. [CrossRef]
9. Gentry, S.P.; Halloran, J.W. Depth and Width of Cured Lines in Photopolymerizable Ceramic Suspensions. *J. Eur. Ceram. Soc.* **2013**, *33*, 1981–1988. [CrossRef]
10. Hinczewski, C.; Corbel, S.; Chartier, T. Ceramic Suspensions Suitable for Stereolithogiaphy. *J. Eur. Ceram. Soc.* **1998**, *18*, 583–590.
11. Rwei, S.P.; Chen, J. Da Investigating the UV-Curing Performance for Polyacrylated Polymer in Dendritic and Regular Conformation. *Polym. Bull.* **2012**, *68*, 493–505. [CrossRef]
12. Uhl, F.M.; Webster, D.C.; Davuluri, S.P.; Wong, S.C. UV Curable Epoxy Acrylate-Clay Nanocomposites. *Eur. Polym. J.* **2006**, *42*, 2596–2605. [CrossRef]
13. Bergoglio, M.; Najmi, Z.; Cochis, A.; Miola, M.; Vernè, E.; Sangermano, M. UV-Cured Bio-Based Acrylated Soybean Oil Scaffold Reinforced with Bioactive Glasses. *Polymers* **2023**, *15*, 4089. [CrossRef]
14. Cheng, Q.; Zheng, Y.; Wang, T.; Sun, D.; Lin, R. Yellow Resistant Photosensitive Resin for Digital Light Processing 3D Printing. *J. Appl. Polym. Sci.* **2020**, *137*, 48369. [CrossRef]
15. Stampfl, J.; Wöß, A.; Seidler, S.; Fouad, H.; Pisaipan, A.; Schwager, F.; Liska, R. Water Soluble, Photocurable Resins for Rapid Prototyping Applications. *Macromol. Symp.* **2004**, *217*, 99–108. [CrossRef]
16. Li, H.; Liu, Y.; Liu, Y.; Hu, K.; Lu, Z.; Liang, J. Effects of Solvent Debinding on the Microstructure and Properties of 3D-Printed Alumina Ceramics. *ACS Omega* **2020**, *5*, 27455–27462. [CrossRef] [PubMed]
17. Xie, H.; Basu, S.; Demeter, E.C. Combining FDTD and Curing Kinetic Equations to Model the Degree of Conversion Evolution of UV-Curable Systems. *Ind. Eng. Chem. Res.* **2021**, *60*, 7174–7186. [CrossRef]
18. Peterson, G.I.; Schwartz, J.J.; Zhang, D.; Weiss, B.M.; Ganter, M.A.; Storti, D.W.; Boydston, A.J. Production of Materials with Spatially-Controlled Cross-Link Density via Vat Photopolymerization. *ACS Appl. Mater. Interfaces* **2016**, *8*, 29037–29043. [CrossRef]
19. Cramer, C.L.; Wilt, J.K.; Campbell, Q.A.; Han, L.; Saito, T.; Nelson, A.T. Accuracy of Stereolithography Printed Alumina with Digital Light Processing. *Open Ceram.* **2021**, *8*, 100194. [CrossRef]
20. Ye, C.C.; Ru, H.Q.; Zhang, C.P.; Wang, W.; Chen, D.L. Fracture Toughness of Si3N4 Ceramic Composites: Effect of Texture. *J. Eur. Ceram. Soc.* **2021**, *41*, 6346–6355. [CrossRef]
21. Yared, W.; Gadow, R. Elimination of Delamination Cracks in Ceramics Manufactured Using LCD Stereolithography. *Open Ceram.* **2024**, *17*, 100531. [CrossRef]
22. Chen, S.; Wang, C.S.; Zheng, W.; Wu, J.M.; Yan, C.Z.; Shi, Y.S. Effects of Particle Size Distribution and Sintering Temperature on Properties of Alumina Mold Material Prepared by Stereolithography. *Ceram. Int.* **2022**, *48*, 6069–6077. [CrossRef]
23. Hofer, A.K.; Kocjan, A.; Bermejo, R. High-Strength Lithography-Based Additive Manufacturing of Ceramic Components with Rapid Sintering. *Addit. Manuf.* **2022**, *59*, 103141. [CrossRef]
24. Chai, J.; Zhu, Y.; Shen, T.; Liu, Y.; Niu, L.; Li, S.; Jin, P.; Cui, M.; Wang, Z. Assessing Fracture Toughness in Sintered Al_2O_3–ZrO_2(3Y)–SiC Ceramic Composites through Indentation Technique. *Ceram. Int.* **2020**, *46*, 27143–27149. [CrossRef]
25. Lam, B.C.; Kassner, C.T.; Kemp, J.W.; Leicht, B.T.; Bohan, B.T.; Rueschhoff, L.M. Delamination Mitigation in Additively Manufactured Al_2O_3 via Enhanced Thermal Postprocessing. *Int. J. Appl. Ceram. Technol.* **2024**, *21*, 675–685. [CrossRef]
26. Zhang, K.; He, R.; Ding, G.; Bai, X.; Fang, D. Effects of Fine Grains and Sintering Additives on Stereolithography Additive Manufactured Al_2O_3 Ceramic. *Ceram. Int.* **2021**, *47*, 2303–2310. [CrossRef]
27. Klimera, A.; Raether, F.; Schulze Horn, P. In Situ Investigation of Debinding of Non-Oxide Ceramic. In Proceedings of the 11th International Ceramics Congress, Sicily, Italy, 4–9 June 2006; Trans Tech Publications Ltd.: Bäch, Switzerland, 2006; Volume 45, pp. 1684–1689.
28. Zocca, A.; Günster, J. Towards a Debinding-Free Additive Manufacturing of Ceramics: A Development Perspective of Water-Based LSD and LIS Technologies. *Open Ceram.* **2024**, *19*, 100632. [CrossRef]
29. Komissarenko, D.A.; Sokolov, P.S.; Evstigneeva, A.D.; Shmeleva, I.A.; Dosovitsky, A.E. Rheological and Curing Behavior of Acrylate-Based Suspensions for the DLP 3D Printing of Complex Zirconia Parts. *Materials* **2018**, *11*, 2350. [CrossRef]
30. Large Amplitude Oscillatory Shear Rheology of Pickering Emulsions. eScholarship, University of California, n.d. Available online: https://escholarship.org/uc/item/0408k3fg (accessed on 19 January 2026).
31. Diptanshu; Miao, G.; Ma, C. Vat Photopolymerization 3D Printing of Ceramics: Effects of Fine Powder. *Manuf. Lett.* **2019**, *21*, 20–23. [CrossRef]
32. Coppola, B.; Fiume, E.; Terranova, V.; Montanaro, L.; Palmero, P. Digital Light Processing of Ceria-Stabilized Zirconia: Role of Powder Pre-Treatment on Printability and Physico-Mechanical Properties. *J. Eur. Ceram. Soc.* **2025**, *45*, 117512. [CrossRef]
33. Lima, L.K.S.; Silva, K.R.; Menezes, R.R.; Santana, L.N.L.; Lira, H.L. Microstructural Characteristics, Properties, Synthesis and Applications of Mullite: A Review. *Ceramica* **2022**, *68*, 126–142. [CrossRef]

34. Salomão, R.; Fernandes, L.; Spera, N.C.M. Combined Effects of SiO_2 Ratio and Purity on Physical Properties and Microstructure of in Situ Alumina-Mullite Ceramic. *Int. J. Appl. Ceram. Technol.* **2021**, *18*, 1702–1709. [CrossRef]
35. Schneider, H.; Fischer, R.X.; Schreuer, J. Mullite: Crystal Structure and Related Properties. *J. Am. Ceram. Soc.* **2015**, *98*, 2948–2967. [CrossRef]
36. Saruhan, B.; Albers, W.; Schneider, H.; Kaysser, W.A. Reaction and Sintering Mechanisms of Mullite in the Systems Cristobalite/α-Al_2O_3 and Amorphous SiO_2/α-Al_2O_3. *J. Eur. Ceram. Soc.* **1996**, *16*, 1075–1081.
37. DiReda, N.; D'Orazio, G.; Sobhani, S. Thermal and Structural Performance of Additively Manufactured Ceramic Porous Media Burners. *J. Eur. Ceram. Soc.* **2024**, *44*, 2271–2279. [CrossRef]
38. Milovanov, Y.; Bertero, A.; Coppola, B.; Palmero, P.; Tulliani, J.-M. Mullite 3D Printed Humidity Sensors. *Ceramics* **2024**, *7*, 807–820. [CrossRef]
39. Bertero, A.; Schmitt, J.; Kaper, H.; Coppola, B.; Palmero, P.; Tulliani, J.-M. MOFs Functionalization of 3D Printed Mullite Complex Architectures for CO_2 Capture. *Appl. Mater. Today* **2024**, *40*, 102407. [CrossRef]
40. Bertero, A.; Coppola, B.; Milovanov, Y.; Palmero, P.; Schmitt, J.; Tulliani, J.-M. DLP 3D-Printed Mullite Ceramics for the Preparation of MOFs Functionalized Monoliths for CO_2 Capture. *Ceramics* **2024**, *7*, 1810–1835. [CrossRef]
41. Bertero, A.; Coppola, B.; Schmitt, J.; Gimello, O.; Trens, P.; Palmero, P.; Tulliani, J.-M. 3D Printed Mullite Monoliths with Triply Periodic Minimal Surface (TPMS) Architectures Functionalized with HKUST-1 for CO_2 Capture. *Microporous Mesoporous Mater.* **2025**, *390*, 113601. [CrossRef]
42. Wu, R.; Wang, C.; Xu, G.; Fan, M.; Huang, Z.; Zeng, T.; Wang, X. Preparation and Characteristics of Porous Mullite Ceramics by 3D Printing and In-Situ Synthesis. *Materials* **2025**, *18*, 956. [CrossRef] [PubMed]
43. EL-Rafei, A.M.; Mansour, T.S. Physico-Mechanical and Microstructure Characteristics of Porous Mullite Ceramics. *Silicon* **2023**, *15*, 7157–7170. [CrossRef]
44. Sintered Mullite—Jiangsu Jingxin New Materials Co., Ltd. Available online: https://www.jxrefractory.com/product/sintered-mullite.html (accessed on 19 January 2026).
45. Montanaro, L.; Tulliani, J.M.; Perrot, C.; Negro, A. Sintering of Industrial Mullites. *J. Eur. Ceram. Soc.* **1997**, *11*, 1715–1723. [CrossRef]
46. EPFL. *Travaux Pratiques MXIII—Céramiques et Colloïdes—TP1 (English Version 2017)*; École Polytechnique Fédérale de Lausanne: Lausanne, Switzerland, 2017. Available online: https://www.epfl.ch/labs/lmc/wp-content/uploads/2018/06/TP1_English-_Version-2017.pdf?utm (accessed on 19 January 2026).
47. Gabdullin, A.N.; Molodykh, A.S.; Nikonenko, E.A.; Nikitina, E.V.; Tkacheva, V.E.; Nevolina, O.A. High-Temperature Hydrolysis of Magnesium Nitrate Hexahydrate. *Russ. Metall. (Met.)* **2017**, *2017*, 627–630. [CrossRef]
48. ADMATEC—Admaflex 130 Ceramic and Metal 3D Printer for Additive Manufacturing of Sinterable Ceramics and Metals. Available online: https://admateceurope.com/admaflex130 (accessed on 19 November 2021).
49. Zhang, X.; Xu, Y.; Li, L.; Yan, B.; Bao, J.; Zhang, A. Acrylate-Based Photosensitive Resin for Stereolithographic Three-Dimensional Printing. *J. Appl. Polym. Sci.* **2019**, *136*, 47487. [CrossRef]
50. Montanaro, L.; Perrot, C.; Esnouf, C.; Thollet, G.; Fantozzi, G.; Negro, A. Sintering of Industrial Mullites in the Presence of Magnesia as a Sintering Aid. *J. Am. Ceram. Soc.* **2000**, *83*, 189–196. [CrossRef]
51. Kurosawa, R.; Takeuchi, M.; Ryu, J. Fourier-Transform Infrared and X-Ray Diffraction Analyses of the Hydration Reaction of Pure Magnesium Oxide and Chemically Modified Magnesium Oxide. *RSC Adv.* **2021**, *11*, 24292–24311. [CrossRef]
52. Cividanes, L.S.; Campos, T.M.B.; Rodrigues, L.A.; Brunelli, D.D.; Thim, G.P. Review of Mullite Synthesis Routes by Sol-Gel Method. *J. Solgel Sci. Technol.* **2010**, *55*, 111–125. [CrossRef]
53. Beran, A.; Voll, D.; Schneider, H. Dehydration and Structural Development of Mullite Precursors: An FTIR Spectroscopic Study. *J. Eur. Ceram. Soc.* **2001**, *21*, 2479–2485. [CrossRef]
54. Gören, R.; Ersoy, B.; Özgür, C.; Alp, T. Colloidal Stability-Slip Casting Behavior Relationship in Slurry of Mullite Synthesized by the USP Method. *Ceram. Int.* **2012**, *38*, 679–685. [CrossRef]
55. Tan, H.; Ding, Y.; Yang, J. Mullite Fibres Preparation by Aqueous Sol-Gel Process and Activation Energy of Mullitization. *J. Alloys Compd.* **2010**, *492*, 396–401. [CrossRef]
56. Leão Andrade, Â.; Maria, R.; Turchetti-Maia, M.; Lopes, T.P.; Salas, C.E.; Domingues, R.Z. In Vitro Bioactivity and Cytotoxicity of Chemically Treated Glass Fibers. *Mater. Res.* **2002**, *7*, 635–638. [CrossRef]
57. Sulaiman, M.; Rahman, A.A.; Mohamed, N.S. Structural, Thermal and Conductivity Studies of Magnesium Nitrate-Alumina Composite Solid Electrolytes Prepared via Sol-Gel Method. *Int. J. Electrochem. Sci.* **2013**, *8*, 6647–6655. [CrossRef]
58. Liu, Y.; Yang, Z.; Desyaterik, Y.; Gassman, P.L.; Wang, H.; Laskin, A. Hygroscopic Behavior of Substrate-Deposited Particles Studied by Micro-FT-IR Spectroscopy and Complementary Methods of Particle Analysis. *Anal. Chem.* **2008**, *80*, 633–642. [CrossRef] [PubMed]
59. de Camargo, I.L.; Morais, M.M.; Fortulan, C.A.; Branciforti, M.C. A Review on the Rheological Behavior and Formulations of Ceramic Suspensions for Vat Photopolymerization. *Ceram. Int.* **2021**, *47*, 11906–11921. [CrossRef]

60. Tangsathitkulchai, C.; Austin, L.G. Rheology of Concentrated Slurries of Particles of Natural Size Distribution Produced by Grinding. *Powder Technol.* **1988**, *56*, 293–299. [CrossRef]
61. Kumar Senapati, P.; Parida, A. Predicting Viscosity of Limestone-Water Slurry. *J. Miner. Mater. Charact. Eng.* **2009**, *8*, 203–221. [CrossRef]
62. Olhero, S.M.; Ferreira, J.M.F. Influence of Particle Size Distribution on Rheology and Particle Packing of Silica-Based Suspensions. *Powder Technol.* **2004**, *139*, 69–75. [CrossRef]
63. Zhang, H.; Wang, H.; Gu, H.; Zong, X.; Tu, B.; Xu, P.; Wang, B.; Wang, W.; Liu, S.; Fu, Z. Preparation of Transparent $MgO{\cdot}1.8Al_2O_3$ Spinel Ceramics by Aqueous Gelcasting, Presintering and Hot Isostatic Pressing. *J. Eur. Ceram. Soc.* **2018**, *38*, 4057–4063. [CrossRef]
64. Li, X.; Zhong, H.; Zhang, J.; Duan, Y.; Bai, H.; Li, J.; Jiang, D. Dispersion and Properties of Zirconia Suspensions for Stereolithography. *Int. J. Appl. Ceram. Technol.* **2020**, *17*, 239–247. [CrossRef]
65. Scherzer, T.; Decker, U. Real-Time FTIR-ATR Spectroscopy to Study the Kinetics of Ultrafast Photopolymerization Reactions Induced by Monochromatic UV Light. *Vib. Spectrosc.* **1999**, *19*, 385–398. [CrossRef]
66. Scherzer, T.; Decker, U. The Effect of Temperature on the Kinetics of Diacrylate Photopolymerizations Studied by Real-Time FTIR Spectroscopy. *Polymer* **2000**, *41*, 7681–7690. [CrossRef]
67. Volle, N.; Giulieri, F.; Burr, A.; Pagnotta, S.; Chaze, A.M. Controlled Interactions between Silanol Groups at the Surface of Sepiolite and an Acrylate Matrix: Consequences on the Thermal and Mechanical Properties. *Mater. Chem. Phys.* **2012**, *134*, 417–424. [CrossRef]
68. Ajiboye, G.I.; Jessop, J.L.P. Synergistic Effect of Hydroxyl-Containing Acrylates in Epoxide-Acrylate Hybrid Photopolymerizations. In Proceedings of the 2012 RadTech UV&EB Technology & Conference, Chicago, IL, USA, 30 April–2 May 2012; pp. 1–6. Available online: https://www.radtech.org/proceedings/2012/papers/Session%209%20-%20Chemistry/GAjiboye_UIowa.pdf (accessed on 19 January 2026).
69. Lu, X.; Li, Y.; Chen, Z.; Li, S.; Wang, X.; Liu, Q. Recent Trends in Polymer Matrix Solid Buoyancy Materials: A Review. *Polymers* **2024**, *16*, 2307. [CrossRef]
70. Durability of Photopolymers in 3D Printing with SLA and DLP. Available online: https://www.jellypipe.com/en/blog-news/durability-of-photopolymers-in-3d-printing/#c3441 (accessed on 17 December 2024).
71. Lakhdar, Y.; Tuck, C.; Binner, J.; Terry, A.; Goodridge, R. Additive Manufacturing of Advanced Ceramic Materials. *Prog. Mater. Sci.* **2021**, *116*, 100736. [CrossRef]
72. Shi, Z.A.; Wu, J.M.; Fang, Z.Q.; Mao, C.; Fu, L.X.; Wang, Q.W.; Yang, S.L.; Zhang, J.X.; Shi, Y.S. Particle Surface Oxidation Modification and Particle Gradation Strategy for the Preparation of High-Strength SiC Ceramics via Vat Photopolymerization. *Addit. Manuf.* **2024**, *84*, 104118. [CrossRef]
73. Yu, X.; Zhao, Y.; Wang, Z.; Wang, Y.; Yu, Z.; Zhong, K.; Zhao, J. Microstructure Formation Mechanisms and Property Regulation Methods during Ceramic Additive Manufacturing. *J. Manuf. Process* **2024**, *131*, 1548–1564. [CrossRef]
74. Cucci, A.L.; Vergani, C.E.; Giampaolo, E.T.; Afonso, M.C. Water Sorption, Solubility, and Bond Strength of Two Autopolymerizing Acrylic Resins and One Heat-Polymerizing Acrylic Resin. *J. Prosthet. Dent.* **1998**, *80*, 434–438. [CrossRef] [PubMed]
75. Dei, L.; Mauro, M.; Bitossi, G. Characterisation of Salt Efflorescences in Cultural Heritage Conservation by Thermal Analysis. *Thermochim. Acta* **1998**, *317*, 133–140. [CrossRef]
76. The Evaluation of Water Sorption/Solubility on Various Acrylic Resins—PubMed. Available online: https://pubmed.ncbi.nlm.nih.gov/19212546/ (accessed on 9 October 2025).
77. McCafferty, E.; Zettlemoyer, A.C. Adsorption of Water Vapour on α-Fe_2O_3. *Discuss. Faraday Soc.* **1971**, *52*, 239–254. [CrossRef]
78. Traversa, E. B Ceramic Sensors for Humidity Detection: The State-of-the-Art and Future Developments. *Sens. Actuators B Chem.* **1995**, *23*, 135–156. [CrossRef]
79. Gu, Q.; Wang, H.; Gao, W.; Yu, J.; Zhou, X. Preparation of Large-Size Alumina Ceramic Parts by DLP 3D Printing Using High-Solid-Loading Paste and Optimizing the Debinding Process. *Ceram. Int.* **2023**, *49*, 28801–28812. [CrossRef]
80. Liao, S.; Chen, J.; Huang, C.; Gao, C.; Peng, L.; Huang, Z. Powder Extrusion Printing of Silicon Carbide Ceramics: Optimization of Water-Soluble Binder Systems and Sintering Properties. *J. Eur. Ceram. Soc.* **2025**, *45*, 117167. [CrossRef]